RSC Advances

PAPER

View Article Online
View Journal | View Issue

Check for updates

Cite this: *RSC Adv.*, 2025, **15**, 35677

Synergistic luminescence of Tb^{3+} and Pr^{3+} ions in $Sr_2Y(MoO_4)_4$ for high-resolution optical thermometry

Yosra Bahrouni,[ab] Ikhlas Kachou,[a] Kamel Saidi [ac] and Mohamed Dammak *[a]

Received 30th June 2025
Accepted 22nd September 2025

DOI: 10.1039/d5ra04652a

rsc.li/rsc-advances

Phosphors of the $SrY_2(MoO_4)_4$ series co-doped with Pr^{3+} and Tb^{3+} ions were synthesized and investigated for optical temperature sensing applications. Their structure, morphology, and photoluminescent properties were thoroughly characterized using X-ray diffraction (XRD), field emission scanning electron microscopy (FESEM), UV-vis absorption spectroscopy, and photoluminescence (PL) analysis. The intense dual-mode color-tunable emission revealed prominent transition bands corresponding to $^5D_4 \rightarrow {}^7F_j$ (j = 6, 5, 4, 3) for Tb^{3+} and $^3P_0 \rightarrow {}^3H_6$ and $^3P_0 \rightarrow {}^3F_2$ for Pr^{3+} ions under UV excitation at 450 nm. Chromaticity parameters for both doped and co-doped phosphors were also investigated, demonstrating emissions concentrated in the green and white regions. These properties highlight their potential for applications in solid-state lighting. The synthesized phosphors were further evaluated for their potential in optical temperature sensing based on the fluorescence intensity ratio (FIR) principle. The $SrY_2(MoO_4)_4$: 0.1 Pr^{3+}/0.4 Tb^{3+} phosphors demonstrated strong red emission with a color purity of 85% and achieved a high relative sensitivity of 1.9% K^{-1} for the 488 nm and 648 nm emission ratio, exceeding several reported molybdate-based thermometers, confirming their potential as multifunctional materials for efficient red component generation in solid-state lighting and precise, non-contact optical temperature sensing.

Open Access Article. Published on 26 September 2025. Downloaded on 1/14/2026 4:11:48 PM.
This article is licensed under a Creative Commons Attribution-NonCommercial 3.0 Unported Licence.

Introduction

Temperature is a fundamental physical parameter crucial for assessing heat and cold, significantly impacting many scientific and commercial applications.[1,2] In recent years, there has been an increasing interest in the development of more precise, easy, and economical temperature measuring methods. Conventional techniques are often classified into contact and non-contact procedures. Contact methods necessitate physical touch between the sensor and the item, resulting in possible delays and difficulties in high-temperature settings, whereas non-contact approaches mitigate these constraints and are progressively favored in many domains.[3,4]

For non-contact techniques, optical thermometry has garnered significant attention due to its high precision, low error margin, and cost efficiency.[5] Methods such as emission intensity, fluorescence intensity ratio (FIR), decay lifetime, and emission band shift have been extensively investigated.[6–8] FIR technology, in particular, has emerged as the most popular due to its robust anti-interference capability, accuracy, and operational simplicity.[9,10] This method typically requires two luminescent centers with distinct temperature-dependent responses.[11] As such, phosphors doped with lanthanide ions and transition metals are frequently used in optical temperature sensing, leveraging the impact of temperature variations on their luminescence properties.

Optical temperature sensing using FIR generally involves thermally coupled levels (TCL).[12,13] By employing FIR-based sensors, dependence on external conditions is minimized, enhancing accuracy and resolution. For this purpose, lanthanide ions such as Tb^{3+}, Pr^{3+}, and Ho^{3+} have been widely studied. Selecting a suitable host material is also critical; low phonon energy is preferred to reduce non-radiative transitions.[14,15] Molybdate-based matrices have been widely used owing to their exceptional properties, including high chemical stability, brilliance, high melting point, low toxicity, and long persistence without radioactive radiation.[16–18] In this study, the focus is on $SrY_2(MoO_4)_4$: 0.1 Pr^{3+}/0.4 Tb^{3+} (SYMO: 0.1 Pr^{3+}/0.4 Tb^{3+}) phosphors, synthesized using the solid-state method. Pr^{3+} and Tb^{3+} are well-known for their efficient luminescent properties, with Pr^{3+} emitting green-blue and red light from its $^3P_0$ and $^1D_2$ energy levels to the ground state, and Tb^{3+} predominantly emitting green light from the $^5D_4 \rightarrow {}^7F_x$ transitions (x = 3, 4, 5,

[a]*Applied Physics Laboratory, Faculty of Sciences of Sfax, Department of Physics, University of Sfax, Sfax, Tunisia. E-mail: madidammak@yahoo.fr; mohamed.dammak@fss.usf.tn*

[b]*University of La Laguna, Physics Department, MALTA-Consolider Group, IMN and IUdEA, P. O. Box 456, E-38206 San Cristóbal de La Laguna, Santa Cruz de Tenerife, Spain*

[c]*University of Sfax, Department of Physics, Sfax Preparatory Engineering Institute, 1172 - 3000Sfax, Tunisia*

© 2025 The Author(s). Published by the Royal Society of Chemistry

Open Access Article. Published on 26 September 2025. Downloaded on 1/14/2026 4:11:48 PM.
This article is licensed under a Creative Commons Attribution-NonCommercial 3.0 Unported Licence.

6).[19,20] The luminescence properties of the $^3P_0$ and $^1D_2$ excited states, which decay to the $^3H_4$ ground state, are strongly affected by host lattice parameters such as phonon energy and crystal structure. In certain compounds, however, the $^3P_0$ emission can be entirely suppressed.[21–23]

This study introduces a novel approach to enhance the luminescence efficiency of $Sr_2Y(MoO_4)_4$ (SYMO) phosphors *via* co-doping with Pr^{3+} and Tb^{3+} ions. For the first time, this co-doped system exhibits tunable emissions spanning the green to near-white spectral regions, paving the way for advanced color modulation in photonic materials. Structural and optical characterizations confirm the successful integration of both activator ions into the SYMO host lattice, resulting in efficient and thermally stable luminescence. The optimized SYMO: 0.1 Pr^{3+}/0.4 Tb^{3+} composition demonstrates promising dual-functionality in photoluminescence and high-resolution optical thermometry, positioning it as a strong candidate for applications in smart lighting, white LEDs, and non-contact temperature sensing technologies.

Experimental section

Sample preparation

The Pr^{3+}/Tb^{3+} codoped SYMO phosphors were prepared through a traditional solid state method. First, high purity $SrCO_3$, MoO_3, Y_2O_3, Pr_6O_{11} and Tb_4O_7 were thoroughly grounded in an agate mortar and placed into an alumina crucible. The mixture was pre-calcined at 550 °C for 5 hours to remove volatiles and initiate the reaction. The samples were sintered at 1000 °C for 5 hours in a flowing CO_2 atmosphere. This atmosphere was chosen to help control the oxidation states of Pr^{3+} and Tb^{3+} ions. Although CO_2 is generally considered mildly oxidizing, at high temperatures it can also act in a slightly reducing manner, which helps stabilize the desired oxidation states during the sintering process.

Characterization

The materials were characterized by the use of chosen analytical techniques. The phase purity and crystal structure of samples were identified through powder X-ray diffraction (XRD) patterns on PANalytical X'Pert Pro diffractometer in the Bragg–Brentano geometry. The sample morphologies were examined using a scanning electron microscope (JEOL, JSM 6510LV). Excitation and emission spectra were acquired using a Jobin Yvon Fluoromax-4 spectrofluorometer (Horiba) equipped with a 150 W xenon lamp as the excitation source. To investigate the temperature dependence, photoluminescence spectra were collected with a Horiba Jobin Yvon HR 320 spectrometer, with the sample mounted inside a cryostat.

Results and discussion

Structural study and morphology

Fig. S1 presents the XRD pattern of the synthesized SYMO sample together with the reference data from the JCPDS card no. 82-2369. The observed diffraction peaks match well with those of the pure SYMO phase, confirming good agreement with the standard pattern (JCPDS no. 82-2369).[24] All observed diffraction peaks can be indexed to the tetragonal scheelite-type structure of $Sr_2Y(MoO_4)_4$, As show in Fig. S1, which has a scheelite-type structure in space group $I4_1/a$, indicating that no other impurities are included in the as-obtained sample. Moreover, a Rietveld refinement analysis was performed on the Pr^{3+}/Tb^{3+} doped SYMO samples to improve the clarity of the crystal structure. Fig. 1a shows the results of the refinement. The observed and calculated profiles are in remarkable agreement, indicating the refinement's high accuracy. A comprehensive summary of the structural properties of the samples is given in Table S1. From the figure, we observed that the difference profile of the SYMO was almost flat, indicating a very good fit between observed and calculated profiles. The reliability factor was less than 2, indicating good fitting results and further confirming the phase purity.

Fig. 1b illustrates the morphology of SYMO: 0.1 Pr^{3+}/0.4 Tb^{3+} phosphors, revealing a rod-like one-dimensional structure indicative of anisotropic crystal growth. The rods exhibit an average diameter of about 10 μm and axial lengths extending to several hundred micrometers. These observations suggest that the Pr^{3+}/Tb^{3+} co-doping concentration has little effect on the crystal growth behavior.

Optical characterization

UV-visible. Based on the UV-vis reflectance, the observed emission features may be attributed to the presence of energy levels introduced by Pr^{3+} and Tb^{3+} ions within the host band gap, which facilitate radiative transitions under excitation.[25,26]

The reflectance spectra of pure SYMO, SYMO: 0.4 Tb^{3+}, SYMO: 0.1 Pr^{3+}, and SYMO: 0.1 Pr^{3+}/0.4 Tb^{3+} samples, recorded over the 200–900 nm range, are shown in Fig. 2.

A pronounced absorption band appears in the UV region (200–330 nm), which originates from the Mo–O charge transfer transition, corresponding to electron excitation from the O 2p states to the Mo 4d levels.[27] Moreover, the appearance of bands centered at 446, 487 and 495 nm is monitored and is attributed to the appearance of the transitions: $^3H_4 \rightarrow {}^3P_2$, $^3H_4 \rightarrow {}^3P_1$ and $^3H_4 \rightarrow {}^3P_0$ which related to the Pr^{3+} ions.

In the case of Pr^{3+}, the introduction of 4f states near the valence band can lead to the formation of localized defect levels, effectively narrowing the optical band gap. Additionally, Pr^{3+} can introduce slight lattice distortions due to its ionic radius, which perturbs the Mo–O bonding environment and modifies the electronic band structure. Conversely, Tb^{3+} doping may slightly widen the band gap due to its higher electronegativity and relatively lower interaction with the host valence band states, leading to a modest blue-shift in the absorption edge. These effects reflect the different roles of 4f orbitals and local structural influences introduced by each dopant.

To evaluate the band gap energy, the reflectance spectra were transformed using the Kubelka–Munk function (eqn (1)). Subsequently, the $F(R)$ values were analyzed with the Tauc relation (eqn (2)) in order to estimate the energy separation

© 2025 The Author(s). Published by the Royal Society of Chemistry

Open Access Article. Published on 26 September 2025. Downloaded on 1/14/2026 4:11:48 PM.
This article is licensed under a Creative Commons Attribution-NonCommercial 3.0 Unported Licence.

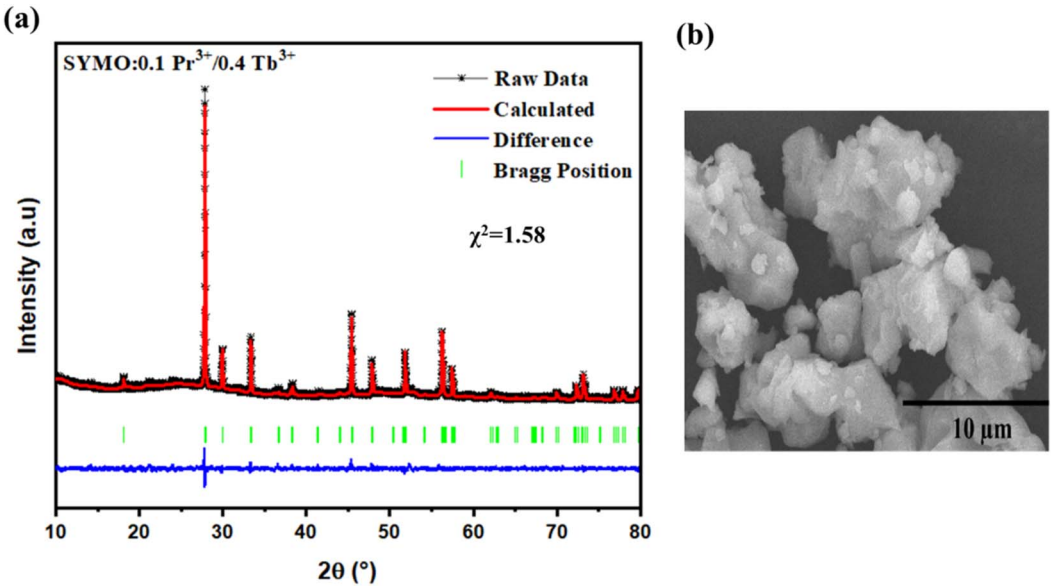

Fig. 1 (a) Rietveld refinement of XRD patterns. (b) SEM images for SYMO codoped 0.1 Pr^{3+}/0.4 Tb^{3+} sample.

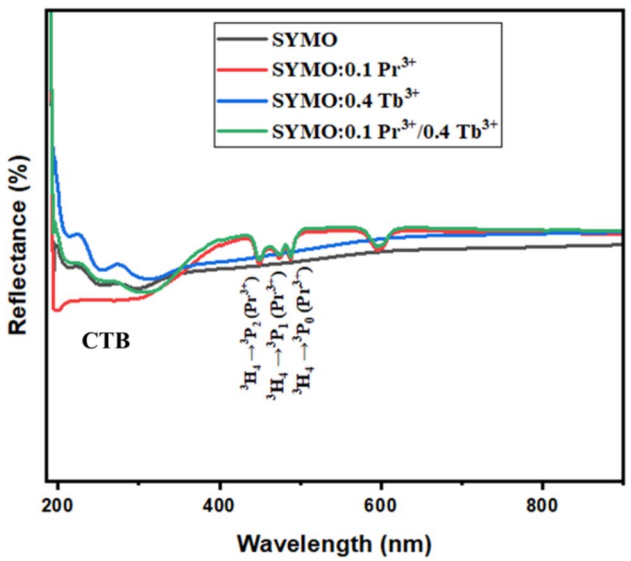

Fig. 2 UV-vis diffuse reflectance spectra of SYMO, SYMO: 0.1 Pr^{3+}, SYMO: 0.4 Tb^{3+} and SYMO: 0.1 Pr^{3+}/0.4 Tb^{3+}.

between the valence band and the conduction band of the synthesized samples, as expressed below:[28,29]

$$F(R) = \frac{(1-R)^2}{2R} = \frac{K}{S} \quad (1)$$

$$(F(R)h\nu)^n = A(h\nu - E_g) \quad (2)$$

The estimated band gap (E_g) values of the samples in this study are 3.5 eV for SYMO, 3.6 eV for SYMO: 0.4 Tb^{3+}, 3.3 eV for SYMO: 0.1 Pr^{3+}, and 3.4 eV for SYMO: 0.1 Pr^{3+}/0.4 Tb^{3+}, as determined by extrapolating the linear region of the plots shown in Fig. S3. These values are consistent with those reported in the literature.[30]

Photoluminescence properties. Fig. 3a displays the PL excitation spectra of the SYMO: 0.4 Tb^{3+} monitored at an emission wavelength of 534 nm. The spectrum shows that the broad band around a wavelength of about 296 nm is attributed to the ligand-to-metal transfer band, which corresponds to the ligand transfer from the O^{2-} ion to the Mo^{6+} ion in the $[MoO4]^{2-}$ groups, and the sharp peaks at 351 nm ($^7F_6 \rightarrow {}^5D_2$), 359 nm ($^7F_6 \rightarrow {}^5G_5$), 369 nm ($^7F_6 \rightarrow {}^5G_6$), 378 nm ($^7F_6 \rightarrow {}^5D_3$) and 486 nm ($^7F_6 \rightarrow {}^5D_5$) are attributed to the transitions of Tb^{3+} ions.[1,31] Upon excitation at 375 nm, as shown in Fig. 3b in the range of 420–520 nm, four PL components (488, 543, 584 and 624 nm) come from the electronic transitions of Tb^{3+} between a excited state ($^5D_4$) and ground states ($^7F_3$, $^7F_4$, $^7F_5$ and $^7F_6$, respectively).[32,33]

Fig. 3c presents the PL excitation spectrum of the SYMO host monitored at an emission wavelength of 620 nm. A wide excitation band is observed between 250 and 320 nm, together with several sharp peaks in the 450–490 nm region. The broad feature centered at 285 nm is attributed to charge transfer from O^{2-} to Mo^{6+} ions.[34,35] Moreover the sharp peaks are ascribed to $^3H_4 \rightarrow {}^3P_2$ (451 nm), $^3H_4 \rightarrow {}^3P_1$ (472 nm) and $^3H_4 \rightarrow {}^3P_0$ (487 nm).[36,37] Upon 450 nm excitation, the studied material shows numerous sharp lines in the 460−760 nm range, the PL spectrum reveals, the emissions peaking at 530 nm, 556 nm, 625 nm, 649 nm corresponding to the $^3P_0 \rightarrow {}^3H_4$, $^3P_1 \rightarrow {}^3H_5$, $^3P_0 \rightarrow {}^3H_6$ and $^3P_0 \rightarrow {}^3F_2$ respectively, while two emissions at 619 nm and 687 nm are attributed to the $^1D_2 \rightarrow {}^3H_4$ and $^1D_2 \rightarrow {}^3H_5$ transitions of Pr^{3+} ions.[38,39] In particular, the blue and orange-red emissions at 556 and 625 nm originate from two thermally coupled levels of $^3P_0$ and $^3P_1$ as shown in Fig. 3b.

Investigation of luminescence in SYMO: 0.1 Pr^{3+}/0.4 Tb^{3+} phosphors. Fig. 4a depicts the excitation spectrum of SYMO: 0.1 Pr^{3+}/0.4 Tb^{3+} microcrystals recorded at 534 nm emission. Strong

Open Access Article. Published on 26 September 2025. Downloaded on 1/14/2026 4:11:48 PM.
This article is licensed under a Creative Commons Attribution-NonCommercial 3.0 Unported Licence.

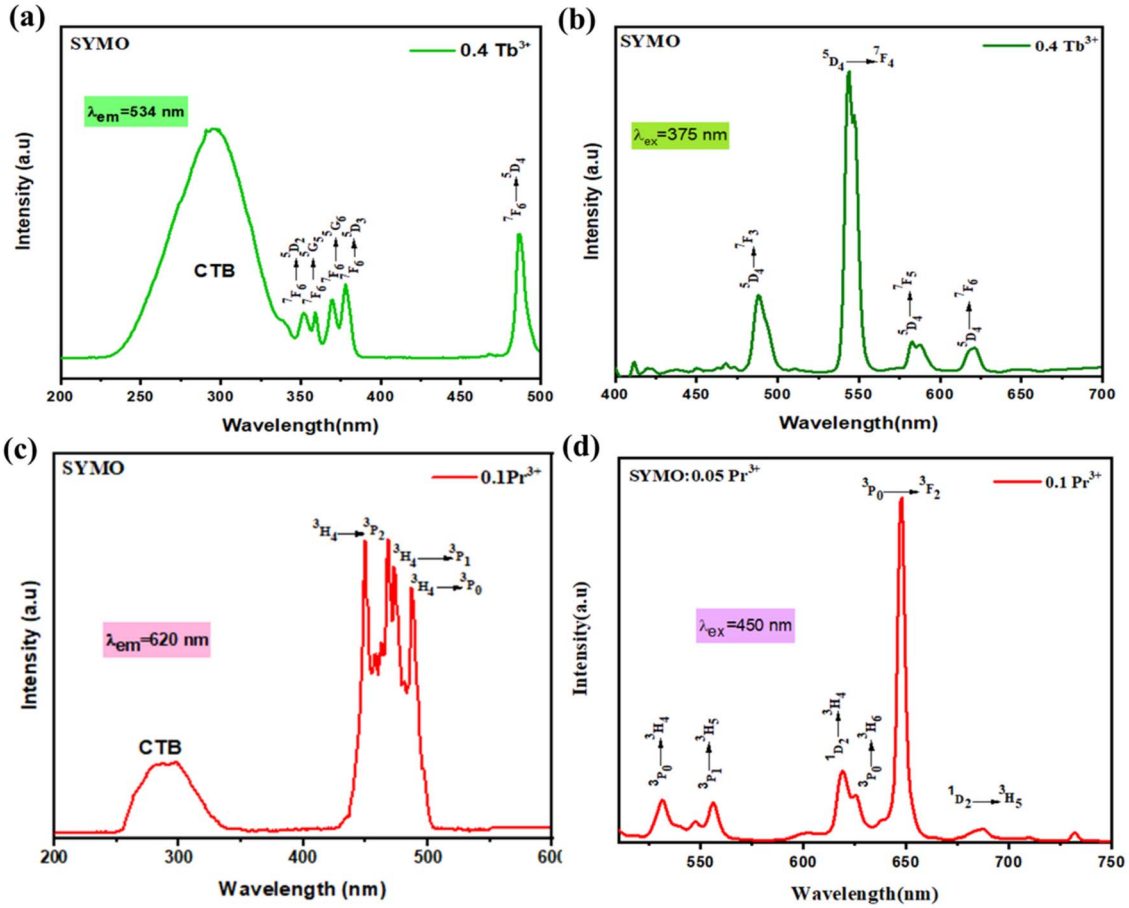

Fig. 3 Excitation and emission spectra (a and b), of the SYMO: 0.4 Tb^{3+} phosphor monitored at 534 nm, and excited at 375 nm, respectively. (c and d), of SYMO: 0.1 Pr^{3+} phosphor monitored at 620 nm, and excited at 450 nm, respectively.

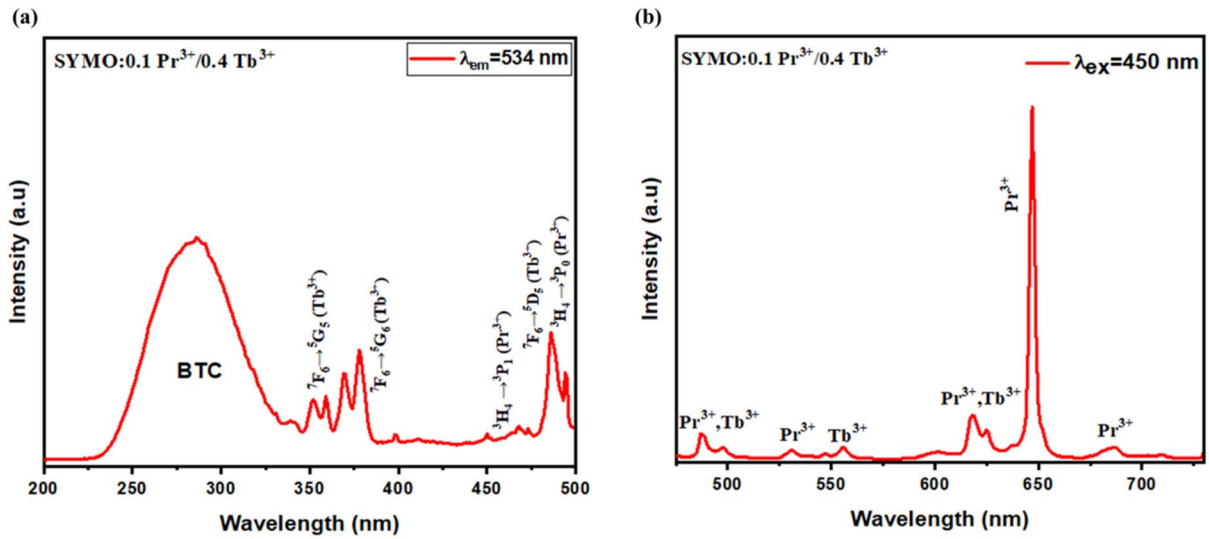

Fig. 4 Excitation and emission spectra of the SYMO: 0.1 Pr^{3+}/0.4 Tb^{3+} phosphors monitored at λ_{em} = 534 nm, and λ_{ex} = 450 nm respectively.

and broad excitation bands appear in the 230–355 nm region, which are assigned to charge–transfer transitions arising from electron transfer between the O^{2-} 2p orbitals and the Mo^{6+} 5d orbitals in the MoO_4 units of the host lattice. In all spectra shown in Fig. 4a, sharp peaks centred at 355 nm ($^7F_6 \rightarrow {}^5D_2$: Tb^{3+}), 375 nm ($^7F_6 \rightarrow {}^5D_3$: Tb^{3+}), 472 nm ($^3H_4 \rightarrow {}^3P_1$: Pr^{3+}) and

© 2025 The Author(s). Published by the Royal Society of Chemistry

Open Access Article. Published on 26 September 2025. Downloaded on 1/14/2026 4:11:48 PM.
This article is licensed under a Creative Commons Attribution-NonCommercial 3.0 Unported Licence.

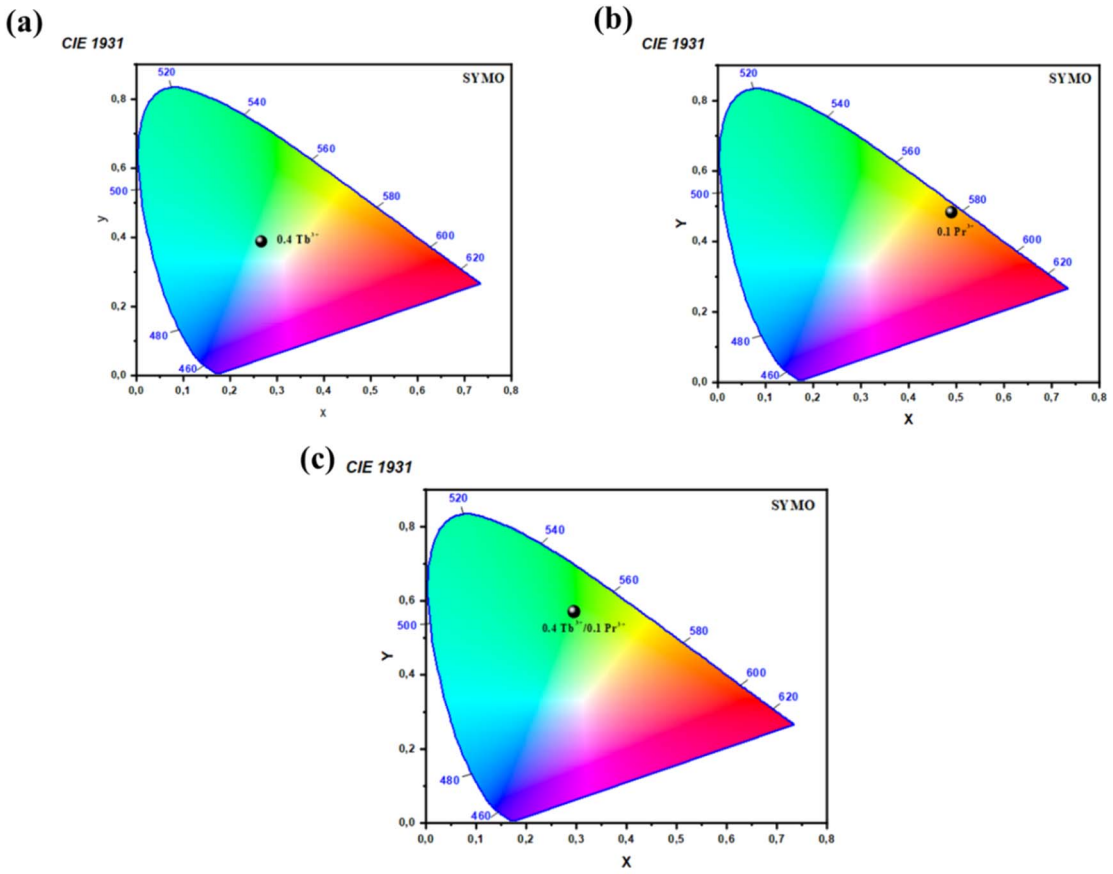

Fig. 5 CIE 1931 chromaticity diagram of SYMO phosphors codoped with (a) 0.4 Tb^{3+}, (b) 0.1 Pr^{3+} and (c) 0.1 Pr^{3+}/0.4 Tb^{3+} excited at λ_{ex} = 450 nm.

486 nm ($^7F_6 \rightarrow {}^5D_5$: Tb^{3+}, $^3H_4 \rightarrow {}^3P_0$: Pr^{3+}) are observed, which were in accordance with those of the doped-only samples. Under 450 nm excitation, Fig. 4b presents the photoluminescence (PL) spectra of SYMO co-doped with Pr^{3+} and Tb^{3+} ions at room temperature. The material exhibits several sharp emission lines corresponding to bands centered at 488 nm (Pr^{3+}, Tb^{3+}), 530 nm (Pr^{3+}), 544 nm (Tb^{3+}), 620 nm (Tb^{3+}, Pr^{3+}), 648 nm (Pr^{3+}) and 689 nm (Pr^{3+}), within the 460–760 nm range.[40–42]

CIE chromaticity coordinates. The CIE chromaticity coordinates (x, y) of the synthesized phosphors under 450 nm UV excitation were calculated and are presented in the CIE chromaticity diagram shown in Fig. 5.[43] The color coordinates and corresponding correlated color temperature (CCT) values of the phosphors are summarized in Table S2. The CCT values were determined from the CIE coordinates using McCamy's formula:[14,44]

$$\mathrm{CCT} = -437n^3 + 3601n^2 - 6861n + 5514.3 \quad (3)$$

$$n = \frac{(x - x_e)}{(y - y_e)}$$

Here, x_e = 0.3320 and y_e = 0.1858 represent the epicenter coordinates of the color.

All samples exhibit CCT values under 3200 K, indicating a warm appearance, as values above 3200 K are usually classified as cool light sources.[45] Fig. 5a shows that the CIE coordinates of SYMO: 0.1Pr^{3+} phosphors fall within the red region. In Fig. 5b, under 375 nm excitation, the CIE coordinates of SYMO: 0.4 Tb^{3+} phosphors are located in the green region. Fig. 5c illustrates that the CIE coordinates of SYMO: 0.1 Pr^{3+}/0.4 Tb^{3+} phosphors lie in the blue region. These coordinates provide a key measure of how the emitted light is perceived and are essential for evaluating the overall emission characteristics of the phosphors.

Thermal stability. Thermal stability is a crucial property for lighting applications, particularly for phosphors used in white LEDs (w-LEDs).[46] High-power LED chips can reach temperatures up to 380 K, at which point luminescence intensity typically decreases significantly. To evaluate the thermal stability of SYMO: 0.1 Pr^{3+}/0.4 Tb^{3+}, PL spectra were recorded under 450 nm excitation at different temperatures, as shown in Fig. S4a. The PL emission profile remains largely unchanged with increasing temperature; however, the intensity of the transitions gradually decreases from 300 K to 380 K due to thermal quenching. Notably, the temperature response differs between the

Open Access Article. Published on 26 September 2025. Downloaded on 1/14/2026 4:11:48 PM.
This article is licensed under a Creative Commons Attribution-NonCommercial 3.0 Unported Licence.

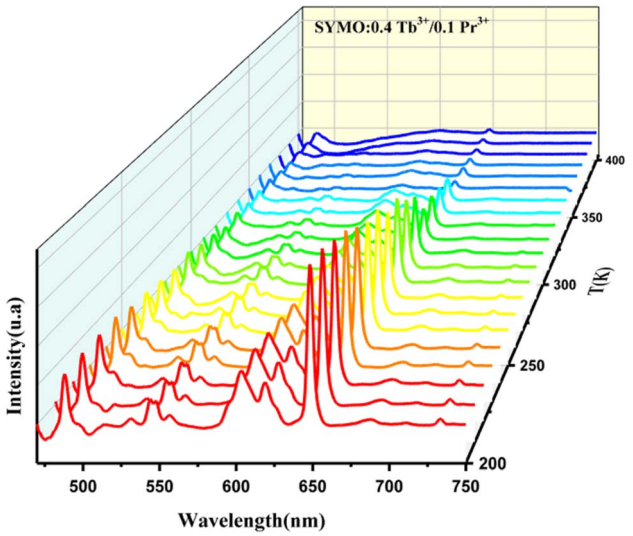

Fig. 6 Temperature-dependent PL spectra of the SYMO phosphor codoped 0.1 Pr^{3+}/0.4 Tb^{3+} excited at 450 nm.

$(MoO_4)^{4-}$ band and the Pr^{3+}/Tb^{3+} bands: the $(MoO_4)^{4-}$ band shows a sharp drop in intensity, whereas the Pr^{3+}/Tb^{3+} emissions decrease more gradually, as illustrated in the histogram of Fig. S4b. Even at 380 K, the luminescence intensity retains 45% of its initial value.

Thermal quenching is primarily caused by non-radiative relaxation, with the number of excited electrons increasing as the temperature rises. This thermal activation process can be quantitatively described using the Arrhenius equation.

$$I(T) = I_0 \left(1 + C \times e^{\frac{-\Delta E}{K_B T}} \right)^{-1} \quad (4)$$

In the equation, I_0 represents the luminescence intensity at room temperature, I is the intensity at elevated temperatures, K denotes the Boltzmann constant, and CCC is a constant. Fig. S4c shows the plot of $(I_0/I - 1)$ *versus* $1/K_BT$, which follows a linear relationship with a slope corresponding to the activation energy, ΔE. From this fitting, the thermal activation energy of SYMO: 0.1 Pr^{3+}/0.4 Tb^{3+} is estimated to be 0.4 eV, confirming the high thermal stability of this phosphor. This value is notably higher than those reported for other phosphors, such as $Lu_2Mo_3O_{12}$: Tb^{3+} (0.29 eV),[47] and $CaYAlO_4$: Tb^{3+} (0.39 eV)[48] further indicating the superior thermal stability of SYMO: 0.1 Pr^{3+}/0.4 Tb^{3+}.

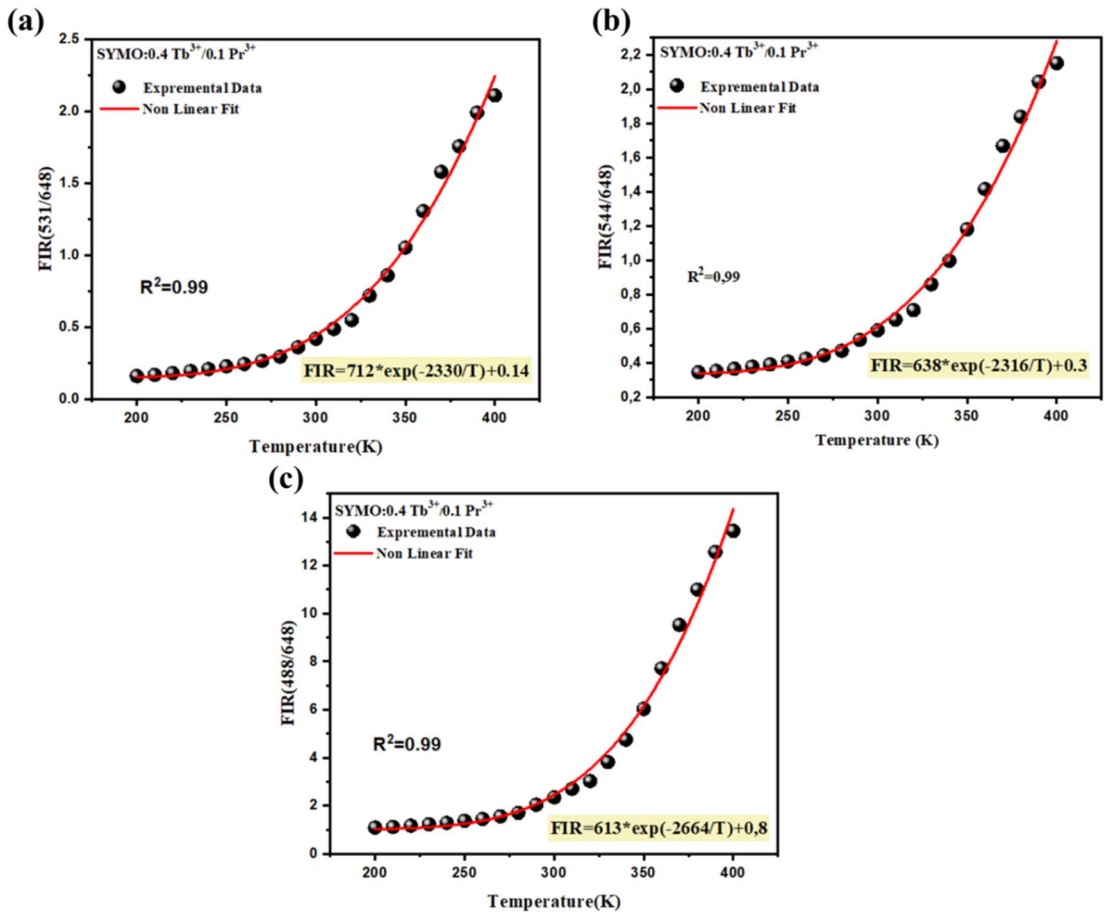

Fig. 7 FIR *vs.* temperature variations for SYMO: 0.1 Pr^{3+}/0.4 Tb^{3+} corresponding to the transition intensity ratios: (a) 488/688 nm, (b) 544/648 nm, and (c) 531/688 nm.

© 2025 The Author(s). Published by the Royal Society of Chemistry

Open Access Article. Published on 26 September 2025. Downloaded on 1/14/2026 4:11:48 PM.
This article is licensed under a Creative Commons Attribution-NonCommercial 3.0 Unported Licence.

Temperature sensing properties

In further evaluation of the potential of the investigated materials for optical temperature sensing, the high-temperature PL spectra of SYMO: 0.1 Pr^{3+}/0.4 Tb^{3+} were measured. It can be seen from Fig. 7 that the total luminescence intensity gradually decreases with the increase of the sample temperature under the excitation of 450 nm, in the range of 215–498 K, indicating that a temperature-dependent luminescence quenching takes place which related to the enhancement probability of the non-radiative processes.[49] Interestingly, the $^3P_0$ and $^1D_2$ related emissions of Pr^{3+} show different temperature responses.[50,51]

The differing temperature responses of Tb^{3+} and Pr^{3+} ions suggest that these phosphors could be used in optical thermometry, with the FIR method serving to assess their performance in real temperature measurements. As illustrated in Fig. 6, the temperature-dependent luminescence property of Pr^{3+}/Tb^{3+} ions in SYMO can be well interpreted by the above kinetic, process since the measured plots of FIR *versus* T are well fitted by equation:[52,53]

$$\mathrm{FIR} = A \times \exp\left(\frac{-\Delta E}{KT}\right) + B \tag{5}$$

where A and B are fitting constants, ΔE is the effective energy difference, and K is the Boltzmann constant. Notably, the SYMO: 0.1 Pr^{3+}/0.4 Tb^{3+} phosphor is suitable for thermal sensing within the temperature range of 215–400 K. The fluorescence intensity ratio (FIR) of the $^3P_0 \rightarrow {}^3H_4$ transition (544 nm) to the $^3P_0 \rightarrow {}^3F_2$ transition (648 nm) can be used for temperature calibration, as these two levels are exclusively associated with Pr^{3+} transitions. Additionally, the FIR of the $^5D_3 \rightarrow {}^7F_3$ transition (Tb^{3+}) to the $^3P_0 \rightarrow {}^3F_2$ transition (Pr^{3+}) is also evaluated. The integrated intensities for FIR values: FIR = I544 nm/I648 nm, FIR = I488 nm/I648 nm, and FIR = I531 nm/I648 nm as a function of temperature are illustrated in Fig. 7.

In all cases, the experimental data were fitted using the exponential function in eqn (5), indicating that the temperature dependence of the FIR follows the Boltzmann distribution. All evaluated FIRs are suitable for thermal sensing, with one particular FIR exhibiting the highest thermometric performance.

Additionally, the absolute sensitivity (S_a) and relative sensitivity (S_r) are key parameters for evaluating the performance of optical thermometers and can be calculated using the following equations:[54,55]

$$S_a = \left|\frac{\delta \mathrm{FIR}}{\delta T}\right| \quad S_r = \frac{1}{\mathrm{FIR}}\left|\frac{\delta \mathrm{FIR}}{\delta T}\right| \tag{6}$$

By plotting S_r against temperature, we observed that a doping concentration of 40% Tb^{3+} combined with 10% Pr^{3+} optimizes thermometric performance. This configuration achieved a maximum S_r at approximately room temperature (RT) in

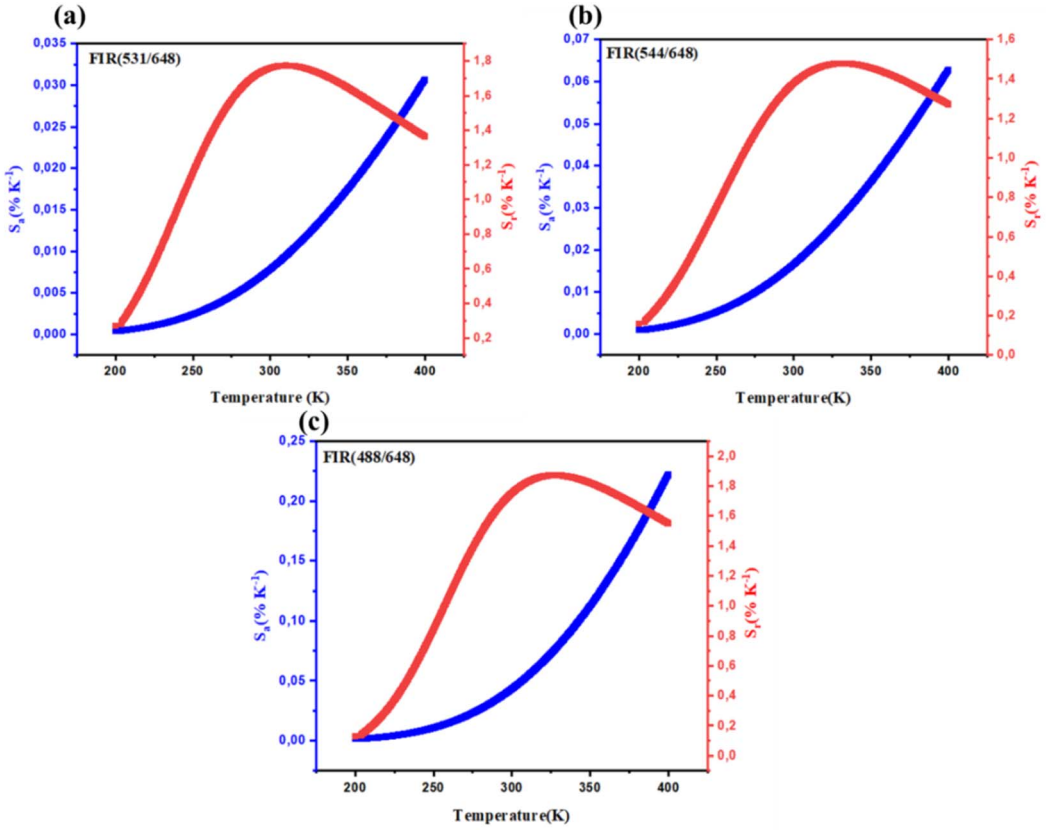

Fig. 8 Variation of temperature sensitivity parameters (absolute and relative sensitivity) as a function of temperature for the SYMO: 0.1 Pr^{3+}/0.4 Tb^{3+} sample, corresponding to the transition intensity ratios: (a) 488/688 nm, (b) 544/648 nm, and (c) 531/688 nm.

Open Access Article. Published on 26 September 2025. Downloaded on 1/14/2026 4:11:48 PM. This article is licensed under a Creative Commons Attribution-NonCommercial 3.0 Unported Licence.

the SYMO crystal, as shown in Fig. 8c corresponding to the FIR (488/648).

The variation in the intensity ratio between emissions at 544 nm and 648 nm yields a sensitivity S_r of 1.5% K^{-1}. Considering the emissions at 488 nm and 648 nm, the S_r increases to 1.9% K^{-1}, while for the lines at 531 nm and 648 nm, the S_r reaches 1.8% K^{-1}, all evaluated at 328 K. The enhanced thermometric performance observed with these intensity ratios is attributed to the greater energy difference between the thermally coupled states.

Besides S_r, temperature resolution δT is one of the most important parameters for FIR thermometry and is denoted as:[56,57]

$$\delta T = \frac{1}{S_R}\frac{\delta \mathrm{FIR}}{\mathrm{FIR}} \quad (7)$$

where δFIR and δFIR/FIR represent the uncertainty and the relative uncertainty of the FIR, respectively. In order to assess the δT of the PL lines at 215 K and 450 K, the FIRs between the integrated intensities of the FIR (544/648), FIR (531/648) and FIR (488/648) emission lines were calculated on the basis of the results. Fig. S5 displays the measured values of the uncertainties at different temperatures for the SYMO sample, and from the graph it is obvious that they are in the range of 0.25–0.5 K, which is an impressive result. A comparison of the sensitivity parameters with previously reported optical thermometry results is presented in Table 1. This analysis highlights the potential of the prepared sample for use in non-contact optical temperature sensing applications.

To evaluate the accuracy of the temperature measurement method, the thermometric parameters (FIR values) were repeatedly measured while cycling the sample between low and high temperatures, as shown in Fig. S6. The repeatability (R) was calculated using the following equation:[58,59]

$$R_p(100\%) = \left(1 - \frac{\max\left|M_i(T)_c - M(T)_c\right|}{\mathrm{FIR}_c} \times 100\right) \quad (8)$$

Here, $M_i(T)_c$ represents the measurement parameter (FIR or band centroid) for the i-th cycle, and $M(T)_c$ is the average value of $M(T)$ over seven cycles. The FIR values exhibit reversible changes with temperature, and all measured FIRs exceeded 97% across the tested temperature range, confirming the excellent repeatability and reliability of the employed thermometric methods.

Table 1 Temperature measurement range, maximum value of S_r of different temperature indicators

Phosphors	Temperature (K)	S_r (% K^{-1})	Reference
$SrMoO_4$:0.01 Pr^{3+}	298–498	0.98	60
YVO_4:0.005 Pr^{3+}	303–324	1.14	61
$SrLu_2O_4$: Pr^{3+}	78–490	1.63	62
$LaMg_{0.4}Nb_{0.5}O_3$: Pr^{3+}	298–523	0.83	63
La_2ZnTiO_6: Tb^{3+}	293–573	0.734	64
$CaWO_4$: Tb^{3+}	343–783	1.21	65
$CaNb_2O_6$:0.01Tb^{3+}/0.5%Bi^{3+}	298–448	1.39	66
$KBaY(MoO_4)_3$: Tb^{3+}/Eu^{3+}	303–503	1.10	67
$SrY_2(MoO_4)_4$: Tb^{3+}/Sm^{3+}	290–440	0.93	68
$NaLu(WO_4)_2$: Tb^{3+}/Pr^{3+}	583–783	1.45	69
$LuNbO_4$: Pr^{3+}/Tb^{3+}	283–493	1.26	70
$Y_2Mo_4O_{15}$: Pr^{3+}/Yb^{3+}	298–508	1.24	71
$SrY_2(MoO_4)_2$: Pr^{3+}/Tb^{3+}	215–400	1.9	This work

Conclusion

In conclusion, the SYMO: 0.1 Pr^{3+}/0.4 Tb^{3+} phosphor series was successfully synthesized *via* the solid-state method. X-ray diffraction confirmed the formation of phase-pure microcrystals with a scheelite-like tetragonal structure. The materials exhibited a wide optical band gap of 3.7 eV, which is consistent with strong host lattice absorption in the UV region and supports efficient excitation of the rare-earth ions under near-UV or blue light (450 nm). These Pr^{3+} activated SYMO phosphors exhibit excellent structural and optical properties, making them promising candidates for optical thermometry. The photoluminescence (PL) spectra revealed a strong contribution from the host matrix under 450 nm excitation, characterized by a broadband profile likely arising from overlapping emissions. Chromatic coordinates derived from the PL spectra place the emissions predominantly in the green and white regions, highlighting their suitability for luminescent applications.

Thermometric characterization, conducted within the 215–400 K range using fluorescence intensity ratio (FIR) techniques, demonstrated the material's effectiveness for precise temperature sensing. Among the various emission pairs analyzed (488/648 nm, 544/648 nm, and 531/648 nm), the I_{488}/I_{648} nm ratio, involving both Tb^{3+} and Pr^{3+} ions, exhibited the best thermometric performance. This pair achieved a maximum sensitivity (S_r) of 1.9% K^{-1} near room temperature (RT), underscoring the material's potential for practical applications in non-contact optical thermometry. Overall, the structural, optical, and thermometric enhancements observed in the SYMO: 0.1 Pr^{3+}/0.4 Tb^{3+} phosphor makes it an excellent candidate for advanced optoelectronic applications, including precise temperature sensing across a wide range of environments. These findings underscore the significant potential of this material for practical use in cutting-edge technologies.

Conflicts of interest

There are no conflicts to declare.

Data availability

All data underlying the results are available as part of the article and no additional source data are required.

Supplementary information: supporting data and analyses, namely XRD patterns, UV-vis diffuse reflectance spectra, Tauc plots, temperature-dependent photoluminescence spectra, FIR-based thermometric performance (including temperature uncertainty and cyclic repeatability), as well as Rietveld refinement data, crystal structure parameters, and CIE chromaticity coordinates of the studied SYMO: Pr^{3+}/Tb^{3+} phosphors. See DOI: https://doi.org/10.1039/d5ra04652a.

© 2025 The Author(s). Published by the Royal Society of Chemistry

Open Access Article. Published on 26 September 2025. Downloaded on 1/14/2026 4:11:48 PM. This article is licensed under a Creative Commons Attribution-NonCommercial 3.0 Unported Licence.

References

1 L. Chen, K. He, G. Bai, H. Xie, X. Yang and S. Xu, *J. Alloys Compd.*, 2020, **846**, 156425H.
2 H. Y. Zhang, G. Li, S. Liu, H. Li, Y. Gong, Y. Liang and Y. Chen, *Chem. Eng. J.*, 2020, **396**, 125251.
3 D. Chen, S. Liu, Y. Zhou, Z. Wan, P. Huang and Z. Ji, *J. Mater. Chem. C*, 2016, **4**, 9044–9051.
4 H. Suo, X. Zhao, Z. Zhang, Y. Wang, J. Sun, M. Jin and C. Guo, *Laser Photonics Rev.*, 2020, **15**, 2000319.
5 S. Senapati and K. K. Nanda, *J. Mater. Chem. C*, 2017, **5**, 1074–1082.
6 M. Behrendt, S. Mahlik, K. Szczodrowski, B. Kuklinski and M. Grinberg, *Phys. Chem. Chem. Phys.*, 2016, **18**, 22266–22275.
7 M. D. Wisser, M. Chea, Y. Lin, D. M. Wu, W. L. Mao, A. Salleo and J. A. Dionne, *Nano Lett.*, 2015, **15**, 1891–1897.
8 Z. E. A. A. Taleb, K. Saïdi, M. Dammak, D. Przybylska and T. Grzyb, *Dalton Trans.*, 2023, **52**, 4954–4963.
9 X. Li, M. Dong, F. Hu, Y. Qin, L. Zhao, X. Wei, Y. Chen, C. Duan and M. Yin, *Ceram. Int.*, 2016, **42**, 6094–6099.
10 A. Zhang, Z. Sun, G. Liu, Z. Fu, Z. Hao, J. Zhang and Y. Wei, *J. Alloys Compd.*, 2017, **728**, 476–483.
11 Z. Antic, M. Dramicanin, K. Prashanthi, D. Jovanovic, S. Kuzman and T. Thundat, *Adv. Mater.*, 2016, **28**, 7745–7752.
12 Y. Cheng, Y. Gao, H. Lin, F. Huang and Y. Wang, *J. Mater. Chem. C*, 2018, **6**, 7462–7478.
13 G. Bao, K. L. Wong, D. Jin and P. A. Tanner, *Light Sci. Appl.*, 2018, **7**, 96.
14 K. Saidi, M. Yangui, C. H. Álvarez, M. Dammak, I. R. M. Benenzuela and M. Runowski, *ACS Appl. Mater. Interfaces*, 2024, **16**, 19137–19149.
15 S. Tomar and C. Shivakumara, *Methods Appl. Fluoresc.*, 2023, **11**, 024001.
16 G. Li, L. Li, M. Li, W. Bao, Y. Song, S. Gan, H. Zou and X. Xu, *J. Alloys Compd.*, 2013, **550**, 1–8.
17 Y. Wang, C. Lin, H. Zheng, D. Sun, L. Li and B. Chen, *J. Alloys Compd.*, 2013, **559**, 123–128.
18 S. F. Wang, K. K. Rao, Y. R. Wang, Y. F. Hsu, S. H. Chen and Y. C. Lu, *J. Am. Ceram. Soc.*, 2009, **92**, 1732–1738.
19 H. Qin, X. Gong, Y. Chen, J. Huang, Y. Lin, Z. Luo and Y. Huang, *J. Lumin.*, 2019, **210**, 52–57.
20 H. Boubekri, M. Diaf, K. Labbaci, L. Guerbous, T. Duvaut and J. P. Jouart, *J. Alloys Compd.*, 2013, **575**, 339–343.
21 W. T. Carnall, P. R. Fields and K. Rajnak, *J. Chem. Phys.*, 1968, **49**, 4424–4442.
22 H. H. Caspers, H. E. Rast and R. A. Buchanan, *J. Chem. Phys.*, 1965, **43**, 2124–2128.
23 J. Liu, Z. Shi, Q. Song, D. Li, N. Li, Y. Xue, J. Xu, J. Xu, Q. Wang and X. Xu, *Opt. Mater.*, 2020, **108**, 110219.
24 S. Cho, *Solid State Sci.*, 2020, **101**, 106155.
25 K. Saidi, M. Dammak, K. Soler-Carracedo and I. R. Martín, *Dalton Trans.*, 2022, **51**, 5108–5117.
26 D. Babu, D. Jagadeesan and T. V. L. Thejaswini, Visible light responsive heterophase Titania monoliths for the fast and efficient photocatalytic decontamination of organic pollutants, *Sci. Rep.*, 2024, **14**, 27441.
27 M. C. Oliveira, J. Andrés, L. Gracia, M. S. M. P. de Oliveira, J. M. R. Mercury, E. Longo and I. C. Nogueira, *Appl. Surf. Sci.*, 2019, **463**, 907–917.
28 H. Zhang, Y. J. Liang, Y. L. Zhu, S. Q. Liu, K. Li, J. Yang and W. Lei, *J. Alloys Compd.*, 2018, **767**, 1030–1040.
29 P. Kubelka and F. Munk-Aussig, *Z. Tech. Phys.*, 1931, **12**, 593–601.
30 Y. Xiang, L. Yang, C. Liao, X. Xiang, X. Tang, H. Tang and J. Zhu, *J. Adv. Ceram.*, 2023, **12**, 848–860.
31 S. Chahar, R. Devi, M. Dalal, M. Bala, J. Dalal, P. Boora, V. B. Taxak, R. Lather and S. P. Khatkar, *Ceram. Int.*, 2019, **45**, 606–613.
32 F. F. Hu, H. L. Gong, G. A. Ashraf, *et al.*, *J. Alloys Compd.*, 2022, **909**, 164776.
33 Y. K. Zheng, T. S. Yang, Y. F. Xiang, *et al.*, *J. Alloys Compd.*, 2022, **911**, 165087.
34 L. Zhao, Z. Xicheng and J. Yuanru, Hydrothermal preparation and photoluminescent property of $LiY(MoO_4)_2$:Pr^{3+} red phosphors for white light-emitting diodes, *J. Rare Earths*, 2015, **33**(1), 33.
35 L. Tang, Q. Meng, W. Sun and S. Lü, Preparation and temperature sensing behavior of $NaY(MoO_4)_2$: Pr^{3+}, Tb^{3+}phosphors, *J. Lumin.*, 2021, **230**, 117728.
36 Y. Gao, F. Huang, H. Lin, J. Xu and Y. S. Wang, *Sens. Actuators, B*, 2017, **243**, 137–143.
37 W. Tang, S. Wang, Z. Li, Y. Sun, L. Zheng, R. Zhang, B. Yang, W. Cao and M. Yu, *Appl. Phys. Lett.*, 2016, **108**, 061902.
38 M. Sojka, M. Runowski, P. Woźny, L. D. Carlos, E. Zych and S. Lis, *J. Mater. Chem. C*, 2021, **9**, 13818–13831.
39 E. Cavalli, F. Angiuli, P. Boutinaud and R. Mahiou, *J. Solid State Chem.*, 2012, **185**, 136–142.
40 L. X. Lovisa, Y. L. R. L. Fernandes, L. M. P. Garcia, B. S. Barros, E. Longo, C. A. Paskocimas, M. R. D. Bomio and F. V. Motta, *Opt. Mater.*, 2019, **96**, 109332.
41 L. L. Tang, Q. Y. Meng, L. Bai, W. J. Sun and C. W. Wang, *J. Lumin.*, 2022, **242**, 118570.
42 D. S. Sun, L. L. Zhang, Z. D. Hao, H. Wu, H. J. Wu, Y. S. Luo, L. Yang, X. Zhang, F. Liu and J. H. Zhang, *Dalton Trans.*, 2020, **49**, 17779.
43 P. Singh, S. Modanwal, H. Mishra and S. B. Rai, *RSC Adv.*, 2023, **13**, 22663–22674.
44 C. S. McCamy, *Color Res. Appl.*, 1992, **17**, 142–144.
45 I. Kachou, K. Saidi, C. Hernandez-Alvarez, M. Dammak and I. R. Martín, *Mater. Adv.*, 2024, **5**, 8280–8293, DOI: **10.1039/d4ma00699b**.
46 J. Qin, C. Hu, B. Lei, J. Li, Y. Liu, S. Ye and M. Pan, *J. Mater. Sci. Technol.*, 2014, **30**, 290–294.
47 N. Huang, G. Lu, B. Bai, Z. Chen, M. Zhang, Y. Li, C. Cao and A. Xie, *Chemosensors*, 2022, **10**(12), 533.
48 Y. Wang, J. Cheng, Z. Wang, Y. Gong, C. Tu, J. Huang, Y. Sun and Y. Yu, *Crystals*, 2022, **12**(12), 1729.
49 D. V. Lapaev, V. G. Nikiforov, V. S. Lobkov, A. A. Knyazev and Y. G. Galyametdinov, A photostable vitrified film based on a terbium(III) β-diketonate complex as a sensing element

Open Access Article. Published on 26 September 2025. Downloaded on 1/14/2026 4:11:48 PM.
This article is licensed under a Creative Commons Attribution-NonCommercial 3.0 Unported Licence.

for reusable luminescent thermometers, *J. Mater. Chem. C*, 2018, **6**, 9475–9481.
50 D. V. Lapaev, V. G. Nikiforov, V. S. Lobkov, A. A. Knyazev and Y. G. Galyametdinov, *J. Mater. Chem. C*, 2018, **6**, 9475–9481, DOI: 10.1039/C8TC01288A.
51 M. Sojka, W. Piotrowski, L. Marciniak and E. Zych, *J. Alloys Compd.*, 2024, **970**, 172662, DOI: 10.1016/j.jallcom.2023.172662.
52 F. Ayachi, K. Saidi, W. Chaabani and M. Dammak, *J. Lumin.*, 2021, **240**, 118451.
53 P. Haro-González, I. R. Martín, N. E. Capuj and F. Lahoz, *Opt. Mater.*, 2010, **32**, 1349–1351, DOI: 10.1016/j.optmat.2010.04.013.
54 S. Jana, A. Mondal, J. Manam and S. Das, *J. Alloys Compd.*, 2020, **821**, 153342.
55 F. Chi, B. Jiang, Z. Zhao, Y. Chen, X. Wei, C. Duan, M. Yin and W. Xu, *Sens. Actuators B-Chem.*, 2019, **296**, 126640.
56 V. Kesarwani and V. K. Rai, *J. Appl. Phys.*, 2022, **132**, 113102.
57 Y. Bahrouni, I. Kachou, K. Saidi, T. Kallel, M. Dammak and I. Mediavilla-Jiménez, *Mater. Adv.*, 2025, **6**, 1307–1318.
58 Z. Wang, M. Jia, M. Zhang, X. Jin, H. Xu and Z. Fu, *Inorg. Chem.*, 2021, **60**, 14944–14951.
59 M. Dai, Z. Fu, Z. Wang and H. Xu, *Chem. Eng. J.*, 2023, **452**, 139133.
60 L. Li, P. Yang, W. Xia, Y. Wang, F. Ling, Z. Cao, S. Jiang, G. Xiang, X. Zhou and Y. Wang, *Ceram. Int.*, 2021, **47**, 769–775.
61 H. Zhou, W. Gao, P. Cai, B. Zhang and S. Li, *Solid State Sci.*, 2020, **104**, 106283.
62 S. Wang, S. Ma, J. Wu, Z. Ye and X. Cheng, *Chem. Eng. J.*, 2020, **393**, 124564.
63 H. Zhang, Z. Y. Gao and G. G. Li, *Chem. Eng. J.*, 2020, **380**, 122491.
64 J. W. Li, J. W. Wang and R. S. Lei, *J. Lumin.*, 2022, **249**, 119047.
65 L. P. Li, F. Qin and L. Li, *J. Lumin.*, 2019, **211**, 258–263.
66 H. Zhang, H. Yang, G. Li, S. Liu, H. Li, Y. Gong, Y. Liang and Y. Chen, *Chem. Eng. J.*, 2020, **396**, 125251.
67 Y. Pan, N. Guo, L. Wang, J. Li, W. Lü and Y. Miao, *ACS Appl. Electron. Mater.*, 2020, **2**, 10–3426, DOI: 10.1021/acsaelm.0c00697.
68 I. Kachou, M. Dammak, S. Auguste, F. Amiard and P. Daniel, *Dalton Trans.*, 2023, **52**, 18233–18246.
69 Y. Wu, H. Suo, X. Zhao, Z. Zhou and C. Guo, *Inorg. Chem. Front.*, 2018, **5**, 2456–2464.
70 Y. F. Wu, H. Suo and X. Q. Zhao, *Inorg. Chem. Front.*, 2018, **5**, 2456–2461.
71 M. Fhoula, K. Saidi, C. Hernandez-Álvarez, K. S. Carracedo, M. Dammak and I. R. Martín, *J. Alloys Compd.*, 2024, **979**, 173537.

© 2025 The Author(s). Published by the Royal Society of Chemistry